Stable nanovesicles formed by intrinsically planar bilayers

Mariana Köber [b,a,1], Sílvia Illa-Tuset [a,1], Lidia Ferrer-Tasies [a,c,1], Evelyn Moreno-Calvo [a], Witold I. Tatkiewicz [a], Natascia Grimaldi [a], David Piña [a], Alejandro Pérez Pérez [a], Vega Lloveras [a,b], José Vidal-Gancedo [a,b], Donatella Bulone [d], Imma Ratera [a,b], Jan Skov Pedersen [e], Dganit Danino [f], Jaume Veciana [a,b], Jordi Faraudo [a,*], Nora Ventosa [a,b,*]

[a] *Institut de Ciència de Materials de Barcelona (ICMAB-CSIC), Campus UAB, Cerdanyola del Vallès, Spain*
[b] *Networking Biomedical Research Networking Center on Bioengineering, Biomaterials and Nanomedicine (CIBER-BBN), Spain*
[c] *Nanomol Technologies SL, Campus UAB, 08193 Cerdanyola del Vallès, Spain*
[d] *Institute of Biophysics, Palermo, National Research Council, Palermo, Italy*
[e] *Department of Chemistry and Interdisciplinary Nanoscience Center (iNANO), Aarhus University, Gustav Wieds Vej, 14, 8000 Aarhus, Denmark*
[f] *CryoEM Laboratory of Soft Matter, Faculty of Biotechnology and Food Engineering, Technion, Haifa 3200003, Israel*

GRAPHICAL ABSTRACT
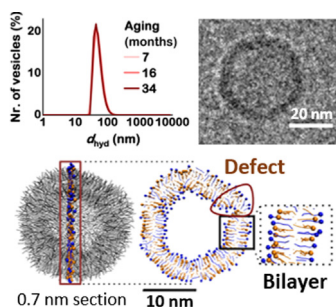
ARTICLE INFO

ABSTRACT

Hypothesis: Quatsome nanovesicles, formed through the self-assembly of cholesterol (CHOL) and cetyltrimethylammonium bromide (CTAB) in water, have shown long-term stability in terms of size and morphology, while at the same time exhibiting high CHOL-CTAB intermolecular binding energies. We hypothesize that CHOL/CTAB quatsomes are indeed thermodynamically stable nanovesicles, and investigate the mechanism underlying their formation.

Experiments: A systematic study was performed to determine whether CHOL/CTAB quatsomes satisfy the experimental requisites of thermodynamically stable vesicles. Coarse-grain molecular dynamics simulations were used to investigate the molecular organization in the vesicle membrane, and the characteristics of the simulated vesicle were corroborated with experimental data obtained by cryo–electron microscopy, small- and wide-angle X-ray scattering, and multi-angle static light scattering.

Findings: CHOL/CTAB quatsomes fulfill the requisites of thermodynamically stable nanovesicles, but they do not exhibit the classical membrane curvature induced by a composition asymmetry between the bilayer leaflets, like catanionic nanovesicles. Instead, CHOL/CTAB quatsomes are formed through the association of intrinsically planar bilayers in a faceted vesicle with defects, indicating that distortions in the organization and orientation of molecules can play a major role in the formation of thermodynamically stable nanovesicles.

© 2022 Published by Elsevier Inc.

---

* Corresponding authors at: Institut de Ciència de Materials de Barcelona (ICMAB-CSIC), Campus UAB, Cerdanyola del Vallès, Spain (N. Ventosa).
E-mail addresses: jfaraudo@icmab.es (J. Faraudo), ventosa@icmab.es (N. Ventosa).
[1] These authors contributed equally to this work.

1. Introduction

The potential of quatsomes has been demonstrated in recent years in a variety of medical applications, for example as scaffolds for creating bright and homogeneous bioimaging and biosensing probes [1–6], inducing the rupture of biofilms [7,8], delivering the recombinant human epidermal growth factor in the treatment of complex wounds [9,10], and delivering small RNAs to treat neuroblastoma [11]. Quatsomes can be functionalized easily by modifying the cholesterol moiety [6,12], and their applicability for intravenous administration has been demonstrated in mice [13]. Over years of use, quatsomes have exhibited remarkable stability in terms of size and morphology, unlike conventional lipid vesicles such as phospholipid liposomes, which led us to investigate its molecular origin.

The organization of amphiphilic molecules in a vesicle-forming self-assembly process can yield thermodynamically stable structures [14–16]. The most prominent example of such stable structures is catanionic vesicles, which are formed by mixtures of cationic and anionic surfactants [17–20]. The theoretical requirements for such stability have been reported to include the presence of a mixed component system exhibiting composition asymmetry between the two bilayer leaflets, thereby yielding spontaneous membrane curvature [21–23]. Recently, theoretical works have described spontaneous membrane curvature arising from asymmetric lipid densities in the two leaflets, but such lipid distributions are thought to be metastable equilibrium states that eventually relax to symmetric lipid densities in both leaflets through flip-flops between the leaflets [24,25]. Also asymmetric ion concentrations across the membrane have been shown to provoke membrane curvature [26,27]. While quatsomes are a mixed component system, it is not known whether they possess such composition asymmetries and spontaneous membrane curvature, related to the mechanism underlying their formation.

In this work, we pursue two interrelated objectives: i) shed light on the mechanism of formation of CHOL/CTAB quatsomes, and ii) determine whether quatsomes are a thermodynamically stable vesicle system. To gain insight into the molecular organization within the quatsome membrane, we performed coarse-grain molecular dynamics (MD) simulations of a full CHOL/CTAB vesicle with an equimolar composition of CHOL and CTAB. We contrasted the characteristics of the simulated vesicle, such as the vesicle diameter, bilayer thickness and disordered liquid-like membrane organization, with experimental observations obtained using cryo–electron microscopy (cryo-EM), small- and wide-angle X-ray scattering (SAXS and WAXS), and multi-angle static light scattering. Furthermore, we checked whether quatsomes satisfy the experimental requisites to be classified as thermodynamically stable vesicles.

2. Materials and methods

2.1. Materials

5-Cholesten-3β-ol (CHOL, purity $\geq$ 95%) was obtained from Panreac AppliChem (Barcelona, Spain). Cetyltrimethylammonium bromide (CTAB, ultra for molecular biology, purity $\geq$ 99%) was purchased from Sigma-Aldrich (Madrid, Spain). All chemicals were used without further purification. The water used was pretreated with the Milli-Q Advantage A10 water purification system (Millipore Ibérica, Madrid, Spain). Ethanol (HPLC grade) was obtained from Teknokroma (Sant Cugat del Vallès, Spain), and carbon dioxide (purity $\geq$ 99.9%) was supplied by Carburos Metálicos S. A. (Barcelona, Spain). 3-β-DOXYL-5α-cholestane was purchased from Santa Cruz Biotechnology (USA).

2.2. Methods for molecular dynamics simulations

Our MD simulations were performed using GROMACS software [28–31] version 2018 and the implicit solvent MARTINI coarse grain force field, known as Dry-MARTINI [32]. All the technical details and protocols of the simulations are described below.

Models and Force Field. The cholesterol and CTAB molecules were modelled using the Dry-MARTINI [29] coarse-grain force field, as shown in Fig. S1. For cholesterol molecules several models compatible with the MARTINI force field are available in the literature. In this work, we employed the model developed by the MARTINI developers [32]. For CTAB we applied the model developed in our group and detailed in Ref. [33].

Building of the initial configuration for MD simulations. In our simulations, we consider as initial condition a pre-built vesicle, to be thermalized and equilibrated in an extended MD run. The initial coordinates for the vesicle were generated using the CHARMM-GUI input generator Martini Maker tool [34,35]. Using this tool, we generated a vesicle with an initial radius of 20 nm and 1:1 cholesterol / surfactant composition. As the CTAB molecule is not available in the CHARMM-GUI tool, our strategy was to select another surfactant molecule with a similar number of Martini beads and then replace the topology of the surfactant molecules by that of CTA$^+$ surfactant before energy minimization (we chose the dodecylpyridinium chloride (DPC) surfactant). The system initially generated with CHARMM-GUI was a spherical vesicle with 2054 cholesterol molecules and 2054 surfactant molecules. After manually substituting the topology of DPC surfactant molecules by CTA$^+$ surfactant, we randomly added 2054 MARTINI anions to neutralize the system charge using the insert-molecules tool from GROMACS package. The system built in this way contained 28756 beads in a cubic simulation box of 31.8 nm length in the three axes. The initial configuration of the system is shown in Fig. S9. This initial structure was energy minimized and thermalized before performing the production runs following the default protocols from CHARMM-GUI.

Protocols for the MD simulation. The equations of motion were solved with a time step of 20 fs. In all our simulations, the temperature was maintained constant (303 K) using the Bussi-Donadio-Parrinello thermostat [36]. We employed periodic boundary conditions in all directions. We observed that an adjustment of the vesicle geometry occurs during the first 100 ns, with the development of planar bilayers and defects form the initially spherical vesicle. In Fig. S10-right, it is clearly observed how the vesicle layers are deformed in comparison with the initial configuration. After this initial time, we performed a production run of 1000 ns and no further changes in the geometry or diameter of the vesicle were observed. The estimated equilibrium diameter is ~18-19 nm (see Fig. 1). The analysis of the simulations was performed using the VMD software [37], and custom scripts to obtain the radial profiles reported in Fig. 1.

2.3. Quatsome production

Quatsome production using ultrasounds (US). Unless otherwise stated, quatsomes were prepared according to the following procedure: For all preparations, the CTAB concentration was kept constant ~10 times above its critical micelle concentration (CMC), at a value of 10 mM. An equimolar ratio of cholesterol was used, i.e. 10 mM. Desired amounts of cholesterol and CTAB were weighted in a flask (38.7 mg and 36.4 mg, respectively), and subsequently suspended in 10 mL of Milli-Q water. Using a Vibracell Sonifier titanium probe working at 20 kHz and a power amplitude of 40% (max. 500 W) (Sonic and Materials Corporation, USA), the resulting dispersion was sonicated at 298 K for 4 minutes, until a homogenous dispersion was obtained.

2.4. Experiments to demonstrate the thermodynamic stability

Quatsome production by CO₂-based processing. Quatsome production via CO$_2$-based processing (DELOS-SUSP methodology) [12,38] consisted of loading a 7.5 mL high-pressure autoclave with a solution of 72.8 mg cholesterol in 2.88 mL ethanol. The solution was heated to the working temperature of 308 K (controlled by an external heating jacket) and then pressurized with compressed CO$_2$ (using a thermostated syringe pump, model 260D, ISCO Inc., Lincoln, US) at a molar fraction of X_{CO_2} = 0.6 until reaching a working pressure of 10 MPa, which produced a volumetric expanded organic solution of cholesterol (a co-solvent behavior of CO$_2$ is observed until X_i = 0.76). The pressurized organic phase was left to equilibrate during one hour at constant pressure. Finally, the CO$_2$-expanded organic phase was depressurized to atmospheric pressure over 24 mL of Milli-Q water containing 68.6 mg of CTAB. To maintain the pressure in the reactor constant during depressurization, N$_2$, pressurized to the working pressure, was used as embolus to push down the expanded solution. The membrane component concentration, prior to process losses, was 5.3 mg/mL (7 mM cholesterol and 7 mM CTAB), and the dispersant contains a volume fraction of 10 % ethanol.

To remove ethanol and excess CTAB, quatsome suspensions were diafiltered using a KrosFlo Research IIi TFF System (Spectrum Labs from Repligen Corporation; Waltham, Massachusetts, USA) equipped with a mPES MicroKros filter column (100 kDa molecular weight cut-off and a surface area of 20 cm^2), at a feed flow rate of 15 mL/min and a transmembrane pressure of about 1.5 psi, unless otherwise noted. Samples were diafiltered applying six cycles of recircularization to ensure the full elimination of all hydrophilic components that were not incorporated in the vesicle membrane.

Spontaneous formation of quatsomes. For the spontaneous formation of quatsomes, we started with CTAB micelles in water and gradually added cholesterol dissolved in ethanol (EtOH). After mixing both, the molarity of CTAB and cholesterol was 7 mM each and the final volume fraction of EtOH 10.7 %. As a first step, stock solutions of CTAB and cholesterol were prepared and equilibrated at 313 K, i.e. well above the Krafft temperature (T_K = 298 K) to assure CTAB micelle formation and also to improve the solubility of cholesterol. In particular, an aqueous solution of CTAB was prepared at 7.8 mM ($\approx$ 7.8 CMC), dissolving 16.25 mg CTAB in 5.7 mL H$_2$O, and a cholesterol solution in ethanol was prepared at 66 mM by dissolving 17.25 mg cholesterol in 0.68 mL EtOH. Subsequently, the cholesterol stock solution was added gradually, in drops of 5 μL, to the aqueous solution containing CTAB micelles, under mild stirring (at the lowest speed that allowed constant stirring, ~ 60 rpm) and while remaining in the 313 K bath. To allow complete equilibration, the sample was left at 313 K with mild stirring for 48 hours.

Reversibility of quatsome formation. To conduct the reversibility experiments, we used quatsomes prepared by DELOS-SUSP. Samples were diafiltered to remove ethanol and excess CTAB. First, we determined the EtOH concentration that entails the complete disintegration of the quatsome membrane and the solubilization of the membrane components. EPR spectra (see below) of quatsomes tagged with the nitroxide spin label 3-β-DOXYL-5α-cholestane in their membranes indicated the complete membrane disintegration at EtOH volume fractions of $\geq$ 50 % (Fig. S5C). Consequently, we fixed the volume fraction of EtOH in the dispersant to 60 % and checked if the reformation of quatsomes occurred upon ethanol evaporation at low pressure. For this, first we determined the evaporation rate of an EtOH-H2O mixture at low pressure, monitoring the changes in the density of the liquid with a pycnometer. We have found that the volume fraction of EtOH was reduced by 6 % per minute at 55 mbar, 311 K and under a slow rotation of the flask. Next, we evaporated the EtOH from the sample containing CTAB and cholesterol using the same experimental conditions. Aliquots were taken at EtOH volume fractions of 30 %, 20 % and 0 %, and all samples were characterized by means of dynamic light scattering (DLS) and cryogenic transmission electron microscopy (cryo-TEM) Fig. S6C.

Note that in the spontaneous formation and DELOS-SUSP processes the presence of some EtOH helps in the vesicle formation process by avoiding the formation of cholesterol crystals, thus facilitating the formation of CHOL/CTAB synthons. However, quatsome vesicles can also be prepared in pure water, i.e. in the absence of any EtOH, as shown in the preparation by ultrasounds, where cholesterol crystals are broken apart through the application of mechanical energy, also facilitating the formation of CHOL/CTAB synthons. We therefore conclude that while the presence of EtOH may help to reach the equilibrium state, equilibrium can be reached likewise in the absence of EtOH. The temporal stability of quatsomes in pure water indicates that this system is stable for years and completely free of precipitates. These experimental observations are in agreement with free energy calculations [39], which have shown a slight preference of a cholesterol molecule to transfer into a 1:1 bilayer membrane (ΔG = -55 kcal/mol) instead of a cholesterol nanocrystal (ΔG = 50 kcal/mol).

Coexistence in equilibrium with neighboring single-phase regions in phase diagrams, i.e. with thermodynamically stable CTAB micelles and cholesterol crystals. To demonstrate the coexistence of quatsomes with CTAB micelles and cholesterol crystals in equilibrium, different molar ratios of CTAB and CHOL were sonicated, following the protocol described above. The CTAB concentration was kept constant ~10 times above its critical micelle concentration (CMC), at a value of 10 mM, and was either mixed with half the cholesterol concentration (5 mM) or with 3/2 of the cholesterol concentration (15 mM). Furthermore, Isothermal titration calorimetry experiments were performed (see below).

2.5. Quatsome characterization

For all characterizations, quatsome preparations were left to stabilize at 298 K for at least 1 week before characterizations were carried out.

Cryo-transmission electron microscopy (cryo-TEM). The morphology of quatsomes was studied by cryo-TEM using two microscopes. Some samples were examined in a JEOL JEM-2011 TEM (JEOL LTD., Tokio, Japan) operating at 120 kV. The samples were vitrified by plunge-freezing in liquid ethane, and storage in liquid nitrogen until loaded onto a cryogenic sample holder (Gatan 626 CTH, Gatan, USA). The working temperature was kept below 98 K. Images were recorded on a Gatan 724 CCD camera under low-dose conditions using the Digital Micrograph 3.9.2. Software package (Gatan Inc.). Other samples were examined using a Tecnai 12 G2 TEM (FEI, USA). Images were recorded on an UltraScan 1000 2k x 2k high resolution CCD camera (Gatan, UK) at up to 50x nominal magnifications, under low dose conditions, following lab protocols [40].

Quantitative analysis of the vesicles' diameters (Fig. 2A) was performed using the ImageJ freeware software. To obtain a statistically relevant size distribution, we have determined the diameter of ~ 8700 spherical vesicles that originated from different experimental batches, all produced under identical experimental conditions, following the protocol for quatsome production by ultrasounds (detailed above). The resolution of the vesicle diameter in cryo-EM images was $\leq$ 2 nm. A Gaussian was fitted to the diameter histogram (bin size 3.5 nm), leaving the mean and standard deviation as fit parameters. The indicated errors of the mean and standard deviation are the standard error of the fit for each parameter.

High-performance liquid chromatography (HPLC). For the determination of the molar ratio of membrane components we have used quatsomes prepared by US and CO_2-based processing. Quatsomes were diafiltered in H_2O to eliminate any excess CTAB not incorporated in the quatsome membrane. All quatsomes systems were disrupted completely before their injection in the HPLC column. With this objective, 1 mL of diafiltered samples (in duplicate or triplicate, as indicated) were lyophilized using a LyoQuest -85 freezedryer (Telstar), with a first freezing step at 193 K for four hours and a subsequent sublimation step at low pressure (0.05 mbar) and increasing temperature. After that, a known volume of organic solvent was added to the lyophilized samples. For the detection of cholesterol and CTAB in the quatsomes we have used an HPLC (1100 series, Agilent Technologies, Santa Clara, CA) equipped with an Evaporative Light Scattering Detector, ELSD (1260 infinity ELSD, Agilent Technologies, Santa Clara, CA). Due to the distinct chemical nature of CTAB and cholesterol we followed two different methods with different columns. Cholesterol separation was carried out using a C18 Symmetry® (5 μm; 4.6 × 150 mm) column (Waters Cromatografía S.A.) at room temperature with an ELSD nebulization temperature of 313 K and evaporative temperature of 353 K. The mobile phase for the cholesterol was a mixture of methanol with water (95:5) (mobile phase A) and formic acid in isopropanol (0.1% HCOOH) (mobile phase B) using gradient flow conditions. For the separation of CTAB we used an InfinityLab Poroshell 120 EC-C18 (4 μm; 4.6 × 100 mm) column (Agilent Technologies) at 308 K with an ELSD nebulization temperature of 313 K and evaporative temperature of 363 K. The mobile phase was a mixture of 50 mM ammonium acetate pH = 3.6 acetic acid (mobile phase A) and acetic acid in methanol (1% HAcO) (mobile phase B) using gradient flow conditions. In the accuracy test of matrix validation, recoveries between of 96–104 % were achieved. The precision, estimated through the relative standard deviation (RSD) in the measurements, was always < 5 %. For both quatsome production methods, the molar ratio between cholesterol and CTAB showed only small deviations from the equimolar ratio (Table S1).

Small-angle X-ray scattering (SAXS). Small-angle X-ray scattering measurements of quatsomes prepared by ultrasounds were performed at the optimized Bruker AXS NanoStar instrument [41,42] at Aarhus University. It uses an Excillum Ga metal jet source operated at 200 W [43] and an optimized collimation section with an octagonal homebuilt scatterless pinhole [44,45] in front of the sample. A homebuilt flow-through cell with an automated sample handler was used for measurements of the samples in a reusable 2.0 mm Ø quartz capillary, which was thermostated using a Peltier element. Typical acquisition time was 2 hrs. The data are displayed as a function of the modulus of the scattering vector $q = 4\pi \sin(\theta)/\lambda$, where 2θ is the scattering angle and λ the wavelength of the X-rays.

Note that the recorded SAXS data in most cases are quite noisy at low q as the vesicles are nearly overall contrast match in SAXS due to the positive-negative electron density contributions to the cross-section structure of nearly the same magnitude. Furthermore, the displayed data are obtained after subtraction of a relatively large background signal from the solvent.

To obtain quantitative information on the vesicle structure from SAXS data, a model of bilayer vesicles with a core-shell structure including overall size polydispersity was fitted to the data using least-squares methods [46]. The cross-section structure was described by three layers, where the central one described the scattering from the electron-poor hydrocarbon part and the two others describe the electron-rich quaternary ammonium groups and counter ions on both sides of the core. To obtain good fits to the data, the sharp box-like cross-section profile was smeared by a Gaussian of width σ_i by multiplying the intensity by exp($-q^2$

σ_i^2).[47] The instrumental smearing of the data due to finite collimation and detector resolution was also estimated and included in the fit by smearing with a resolution function [48]. Fitting of the SAXS data with form factors for structures that deviate from the spherical shape was not considered, since the facet-related 'slip of phase' of the oscillations at high q will barely be observable, as polydispersity smears out the oscillations at higher q [49]. To obtain the outer diameter, the bilayer width (i.e. 5 nm) was added to the diameter for the central plane.

Multi-angle static light scattering (MALS). The molecular weight (Mw) of CHOL/CTAB quatsomes was estimated from MALS measurements in aqueous solution at 298 ± 0.1 K. Samples were placed in a thermostatic cell compartment of a Brookhaven Instrument BI200-SM goniometer, and the temperature was controlled to within 0.1 K using a thermostatic recirculating bath. Upon irradiation with a 100 mW solid-state laser (Quantum-Ventus MPC 6000) tuned at λ = 532 nm the scattered light intensity was measured using a Brookhaven BI-9000 correlator. Measurements were taken at various scattering vectors $q = 4\pi$ n λ_0^{-1} sin $(\theta/2)$, where n is the refractive index of the solution, λ_0 is the wavelength of the incident light, and θ is the scattering angle. Static light scattering data were corrected for the background scattering of the solvent and normalized by using toluene as calibration liquid. All samples were filtered through 200 nm cellulose acetate (MiniSart) syringe filters to remove dust or contaminants. The refractive index increment dn/dc of quatsomes in aqueous solution was determined at 303 K and λ = 620 nm with a (SEC 3010) Brookhaven Instrument differential refractometer. The MALS data (Fig. S4) were analyzed by means of the Zimm plot method and taking into account the measured dn/dc values [50].

Wide-angle X-ray scattering (WAXS). WAXS measurements of quatsomes prepared by ultrasounds were performed at the X33 beamline of the EMBL at 298 K. A sample to detector distance of 1.2 m was used (q range around 3.8–17.5 nm^{-1}), and the wavelength of the beamline was 1.5 Å. WAXS patterns were recorded using a Pilatus 300K-W 2D Photon counting detector. Eight patterns of 30 s each were acquired per sample. Two duplicate measurements of the same batch were performed.

Dynamic light scattering (DLS). The hydrodynamic quatsome diameter was determined using a dynamic light scattering analyzer combined with non-invasive backscatter technology (Malvern Zetasizer Nanoseries, Malvern Instruments, UK). The optimal quatsome concentration for DLS measurements was determined by performing dilutions in Milli-Q water. 10 to 1000-fold dilutions of the as-prepared quatsome suspensions yielded overlapping size distributions, eliminating multiple scattering events observed for undiluted samples. Consequently, all reported data were acquired at 10-fold dilutions. Three consecutive measurements were performed on each sample. Averaged scattering-intensity weighted particle size distributions were determined using the software provided by Malvern, and then converted to number distributions by scaling with R^{-4}. The average hydrodynamic diameter $\bar{d}_{hyd}$ was calculated from the discrete number distribution $n(d_i)$, taking into account the variation of the step length on the logarithmic scale:

$$\bar{d}_{hyd} = \frac{\sum d_i \times n(d_i) \times (d_{i+1} - d_{i-1})/2}{\sum n(d_i) \times (d_{i+1} - d_{i-1})/2}$$

Electron paramagnetic resonance (EPR). For EPR experiments, CHOL/CTAB quatsomes containing the commercial spin probe 3β-DOXYL-5α-cholestane radical at a mol fraction of 1% were produced by DELOS-SUSP, adding the spin probe to the organic phase in the high-pressure autoclave, together with the cholesterol.

EPR spectra were obtained with an X-Band (9.7 GHz) Bruker ELEXSYS E-500 spectrometer equipped with a ST8911 microwave cavity, a Bruker variable temperature unit, a field frequency lock

system Bruker ER 033 M and a NMR Gaussmeter Bruker ER 035 M. The modulation amplitude was kept well below the line width, and the microwave power was well below saturation. We started with the sample of 10% vol. EtOH and then diluted step by step (30%, 40%, 45% vol.) until reaching the 50% in vol. All samples were previously degassed with Ar and measured in a flat quartz EPR cell. The same acquisition parameters were used: microwave power: 2.49 mW; modulation amplitude: 2.0 G; modulation frequency: 100 KHz; receiver gain: 60; time constant: 20.48 ms; conversion time: 40.96 ms; sweep width: 150 G; 15 scans.

Isothermal titration calorimetry (ITC). ITC experiments were performed with a MicroCal VP-ITC System (Malvern Panalytical, UK). The sample cell contained a volume of 1.4 mL of quatsomes, prepared by ultrasounds, with a concentration of CTAB and cholesterol of 50 μM each, thus establishing an equimolar ratio of CHOL/CTAB at the beginning of the experiment. Subsequently, every 300 seconds 5 μL of a CTAB 0.7 mM solution were injected with a syringe, and the heat exchanged per injection was monitored. Blanks consisted in adding 5 μL of the 0.7 mM CTAB solution to H_2O every 300 seconds, as well as adding H_2O to the quatsomes at the above stated concentration. Note that the critical micellar concentration (CMC) of CTAB is approximately 0.9 mM.

Conductivity. The electric conductivity was measured with a Hanna HI 5521 (Hanna Instruments, USA) using a four-ring platinum probe electrode HI76312 (Hanna Instruments, USA). For pure CTAB, a micellar suspension of 5 mM was prepared, and sequentially diluted up to 0.5 mM by adding Milli-Q water (resistivity of 18.2 MΩ*cm). For measurements on CHOL/CTAB quatsomes, sequential dilutions of two different quatsome batches were prepared by adding Milli-Q water. Measurements were performed at different time points up to three days after diluting. For all conductivity measurements the temperature was maintained within ± 0.3 K.

2.6. Calculation of the average number of molecules per vesicle

Calculation from MALS data. The average molecular mass of quatsomes was determined by multi-angle light scattering, yielding $m_{QS} = 13.3 ± 0.8 × 10^6$ g/mol. With a molecular mass of CHOL and CTAB of $m_{CHOL} = 386.65$ g/mol and $m_{CTAB} = 364.45$ g/mol, respectively, and assuming an equimolar composition, the mean number of molecules per vesicle is $N = \frac{m_{QS}}{(m_{CHOL}+m_{CTAB})/2} = 35 ± 2 × 10^3$.

Scaling the simulated vesicle size to the experimentally observed average size. The average bilayer volume $V_{bilayer}^{exp}$ was calculated for an outer vesicle radius R of R_{SAXS} = 23.15 nm and a total bilayer thickness t of t_{SAXS} = 5 nm, both mean values obtained from SAXS: $V_{bilayer}^{exp} = \frac{4}{3}\pi \left(R_{SAXS}^3 - (R_{SAXS} - t_{SAXS})^3 \right)$.

The bilayer volume of the simulated vesicle was equally calculated, with an outer vesicle radius R_{CGMD} = 9 nm and a bilayer thickness of t_{CGMD} = 4 nm: $V_{bilayer}^{sim} = \frac{4}{3}\pi \left(R_{CGMD}^3 - (R_{CGMD} - t_{CGMD})^3 \right)$.

Scaling the number of molecules in the simulated vesicle N_{CGMD} = 4108 to the average volume obtained experimentally, we obtain $N = N_{CGMD} \frac{V_{exp}}{V_{CGMD}} = 44 ± 4 × 10^3$ molecules.

3. Results and discussion

To gain insight into the molecular organization within the quatsome membrane, we performed molecular dynamics (MD) simulations of a full CHOL/CTAB vesicle with an equimolar composition of cholesterol and CTAB (see SI, Fig. S1). We used the implicit solvent Martini coarse-grain force field for lipids [32] and surfactants [33] (nicknamed "Dry Martini"), which has been successfully employed in previous simulations to determine lipid properties, including vesicle formation and fusion [32,51]. The Dry Martini approach

employs a simplified representation of the molecules, wherein on average every 3–4 heavy atoms are replaced by a coarse grain building block (a "bead") with specific chemical interactions parametrized from thermodynamic data. This method enables full vesicle simulations to be conducted with molecular resolution up to the microsecond time scale, well beyond the possibilities of previous atomistic simulations performed on this system [3,39,52].

Our simulations of a 1:1 CHOL/CTAB mixture comprising 4108 molecules at 303 K during ≈ 1 μs predict a vesicular structure, which evidently deviates from a perfectly spherical object. Our results (Fig. 1A–C) clearly indicate that the vesicle is formed through the assembly of planar bilayers, joined together via small defects that provide curvature to the structure, eventually generating a closed vesicle. Cryo-TEM, the best method to directly examine the vesicle morphology at high resolution [40], confirms the presence of these facets and associated slight deviations from a perfectly spherical vesicle shape (Fig. 1D and Fig.S2 (SI)). These deviations become even more evident upon major irradiation, in contrast to phosphatidyl serine liposomes of similar size, which remain round even upon excessive irradiation of > 200 e⁻/Å² that turned the ice crystalline (see SI, Fig. S3). These results substantiate the presence of facets in quatsomes and show that these are different from planar faces present in any vesicle due to thermal fluctuations [53] or in the gel phase.

Importantly, the simulations indicate a uniform distribution of the two components within the leaflets (Fig. 1A), i.e. the absence of any segregation or aggregation of the two components. Moreover, each leaflet contained exactly an equimolar ratio of cholesterol and CTAB (Fig. 1B), and no composition asymmetry existed between the inner and outer leaflet, suggesting that the bilayer curvature did not result from composition asymmetry between the two leaflets. The CHOL/CTAB synthon (bimolecular amphiphile) was found to be present throughout the whole vesicle, maintaining its stable arrangement in the planar regions [39] and exhibiting strong deformations in the defect regions. However, even in the defect regions no segregation of cholesterol or CTAB molecules was observed, and the equimolar ratio was still maintained. On the other hand, on the timescale of the simulation, we found an asymmetric lipid density in the two leaflets, containing 871 synthons in the inner leaflet and 1183 synthons in the outer leaflet.

Overall, our results suggest that the bimolecular CHOL/CTAB synthon forming the membrane [39] has a tendency to form planar bilayers, which in turn form a closed vesicle due to the presence of defect regions that exhibit strong deformations in the molecular orientation of cholesterol and CTAB but no segregation of these two components. This mechanism of vesicle formation is different from that proposed thus far for stable vesicular systems, such as catanionic vesicles, which is based on compositional asymmetry leading to membrane curvature [21,22,54]. Experimentally, we found a ∼10 % deviation from an equimolar composition of the entire vesicular system using high-performance liquid chromatography (see SI, Table S1), which is small compared with the deviations used to produce stable catanionic vesicles, which are generally > 50 % [14,54,55]. In accordance with these results, the size distribution obtained through analyzing the vesicle diameter in cryo-TEM images of more than 8600 vesicles from different experimental batches, despite being roughly Gaussian, exhibited a non-Gaussian tail towards larger sizes (Fig. 2A), thereby pointing towards a vesicle formation mechanism that is not dominated by a spontaneous bilayer curvature resulting from composition asymmetries [54].

It is important to highlight that the characteristics of the simulated vesicle were consistent with several experimental observations: a) The vesicle diameter of ∼18–19 nm (Fig. 1C) corresponds to the smaller quatsomes observed using cryo-TEM (Fig. 2A). b) The bilayer thickness of ∼4 nm (including the surfac-
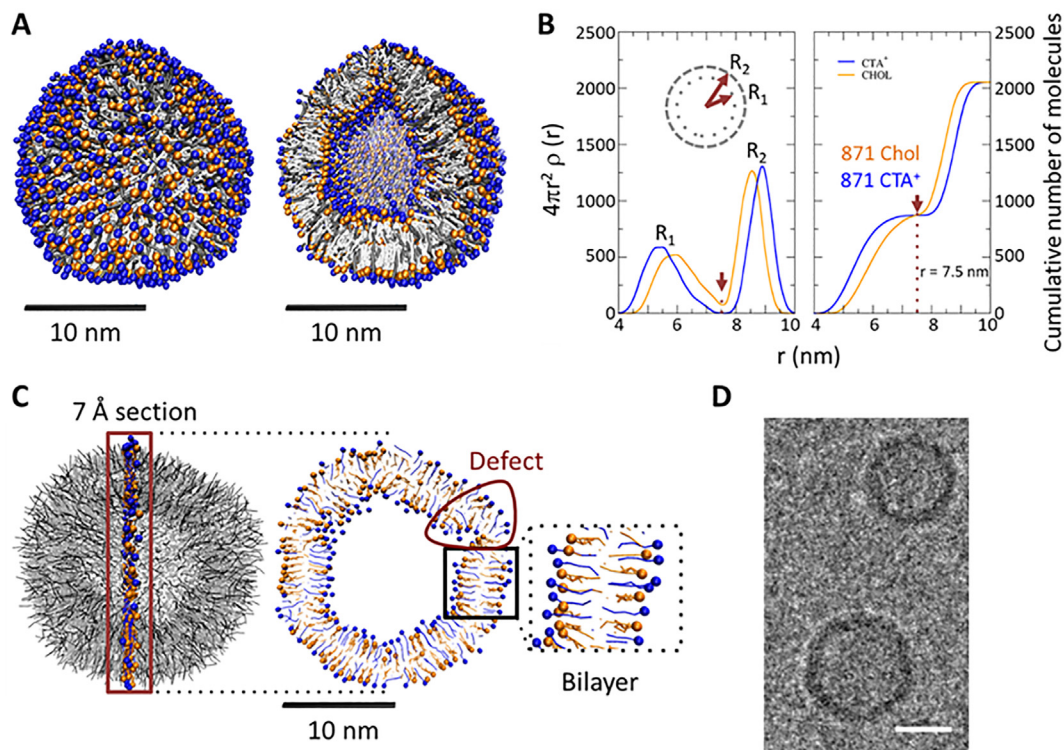
Fig. 1. Molecular composition of bilayer leaflets and supramolecular organization. (A–C) Coarse-grain MD simulation of a CHOL/CTAB quatsome vesicle, at a concentration of 0.1 mM of each component. (A) Snapshot of an equilibrated (303 K) full quatsome vesicle and a cross-section thereof. The head groups of the CTA^+ and cholesterol are depicted as blue and orange balls, respectively (Br^- counterions are omitted for clarity), and their tails are depicted as cylinders. (B) Radial distribution of vesicle components. Left: radial density profile with $\varrho(r)$ calculated as the number of head group beads per nm^3. Right: accumulated (integrated) number of molecules of each component as a function of the radial distance averaged over all equilibrium configurations. The peaks R_1 and R_2 in the CTA^+ head group distribution are also indicated, which correspond to the inner and outer radii of the vesicle, respectively, and the minimum, indicated by an arrow, corresponds to the center of the bilayer. The diameter of the simulated vesicle is estimated as ~ 18–19 nm, taking into account the size of the CTA^+ head group bead (0.47 nm). (C) A detailed snapshot depicting the internal molecular organization of CTA^+ and cholesterol at a 7 Å wide slice of the simulated quatsome vesicle, exposing regions with perfectly ordered planar bilayers (see the enlarged portion of the image) and disordered joining regions, with a 1:1 ratio of the two components. (D) Cryo-TEM image of quatsome vesicles depicting the faceting and deviations from a completely spherical shape (scale bar represents 20 nm). (For interpretation of the references to colour in this figure legend, the reader is referred to the web version of this article.)

tant head groups) (Fig. 1C) is concordant with the value of 4.3 nm obtained in all atomic MD simulations [39] and ∼5 nm obtained experimentally using small-angle X-ray scattering (SAXS) (Fig. 2B). c) The ratio of molecules per bilayer volume is proportional to the experimentally observed value: Scaling the bilayer volume to the average volume obtained experimentally [56], the simulated vesicle would contain $44 \pm 4 \times 10^3$ CTAB and cholesterol molecules, close to the mean value of ca. $35 \pm 2 \times 10^3$, which is obtained experimentally from the molecular weight of 13.3 ± 0.8 MDa determined using multi-angle light scattering (see SI, Fig. S4). d) The molecular organization observed in Fig. 1C is consistent with disordered liquid-like packing, which is also observed experimentally using atomic force microscopy and wide-angle X-ray scattering (see SI, Fig. S5) [3,52].

Because CHOL/CTAB quatsomes exhibit a completely different mechanism of vesicle formation than previously proposed for thermodynamically stable vesicle systems [54,21–27], we aimed to confirm that quatsomes satisfy the experimental requisites of thermodynamically stable vesicles [14], as follows:

i) *The preparation route does not affect the vesicle size.* Regardless of whether quatsomes were prepared through applying ultrasounds (US) or compressed CO_2 (DELOS-SUSP methodology) [12,38], small unilamellar vesicles (insets in Fig. 2A and 3A) with similar size distributions were obtained (Fig. 3A). The somewhat larger polydispersity observed using DLS in comparison with the narrow vesicle size distribution obtained using SAXS (Fig. 2B) and cryo-TEM image analysis (Fig. 2A) was likely due to the large impact of few larger vesicles (visible in cryo-TEM images, Fig. 2A) on the scattered light intensity I

$(I \sim d^4)$. Furthermore, the inter-technique variation in size was within the expected range [58].

ii) *Quatsome size and polydispersity remain stable over time.* Quatsome vesicles maintained their size distribution and unilamellar morphology for years, as observed using DLS and cryo-TEM (Fig. 3B).

iii) *Quatsome formation is reversible upon the change of an external factor.* Quatsome rupture and reformation can be controlled through varying the volume fraction of ethanol in water. When adding EtOH to a quatsome suspension, vesicle rupture occurred at EtOH volume fractions > 30%, which is evident from the analysis of size distribution and cryo-TEM images (see SI, Fig. S6A–B). Complete membrane disintegration took place at volume fractions $\geq$ 50%, as demonstrated through the electron paramagnetic resonance spectra of quatsomes containing the 3β-DOXYL-5α-cholestane radical as spin probe (see SI, Fig. S6C), exhibiting the typical signal corresponding to freely moving nitroxyl radicals (in contrast to the characteristic signature of restricted radical movement observed at low ethanol volume fractions). Upon subsequent ethanol evaporation, quatsome reformation occurred once the EtOH volume fraction was $\leq$ 30% again (Fig. S6A), and at 0% EtOH, we mainly observed small unilamellar vesicles (inset in Fig. 3C) that exhibited a size distribution that overlapped with the distribution obtained prior to the addition of EtOH (Fig. 3C).

iv) *Quatsomes are generated spontaneously.* Quatsome vesicles are formed in the absence of any energy input, simply through the gradual addition of cholesterol dissolved in EtOH to an aqueous solution of CTAB micelles. This procedure yielded small unilamellar vesicles (inset in Fig. 3D) that were similar in size to those
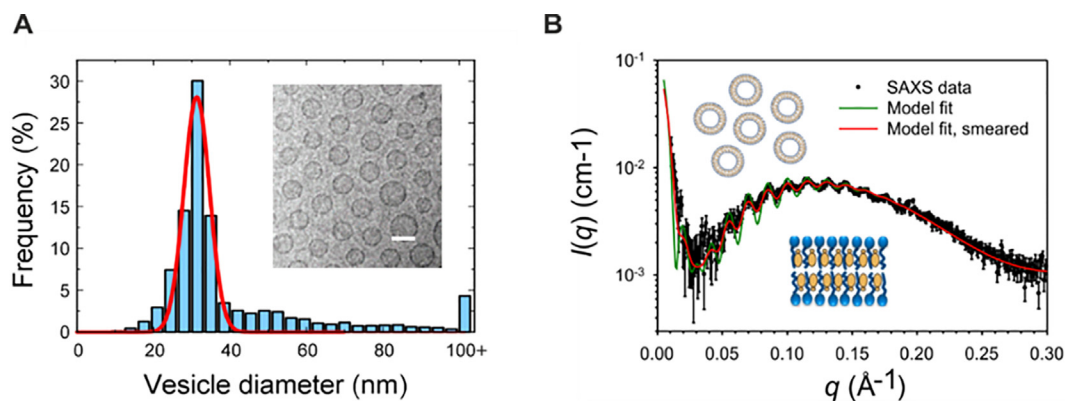
Fig. 2. Relevant geometric characteristics of CHOL/CTAB quatsomes. (A) Vesicle diameter distribution, determined by analyzing cryo-TEM images of 8600 vesicles from various experimental batches, and the Gaussian fit yielding a mean diameter $\overline{d_{TEM}^{Gauss}}$ = 31.4 ± 0.2 nm and a standard deviation of σ_{TEM}^{Gauss} = 3.4 ± 0.2 nm. The arithmetic mean diameter of the entire ensemble is slightly larger, i.e. $\overline{d_{TEM}}$ = 43.2 ± 0.2 nm (mean ± standard error of the mean), due to the presence of few larger vesicles. Inset: Representative cryo-TEM image (scale bar represents 50 nm). (B) SAXS data of CHOL/CTAB quatsomes at a concentration of $\sim$ 6 mM of each component, indicating the scattered intensity as a function of the modulus of the scattering vector q. The broad bump originates from the presence of a three-layer cross-section of the vesicle bilayer, and the oscillations [57] are attributed to the remarkably narrow vesicle size distribution of the overall size, and are generally not observed for conventional vesicles of this size owing to the polydispersity in their size. Fitting the data using a model of bilayer vesicles with an overall size polydispersity [46] yielded an average outer quatsome diameter of d_{SAXS} = 46.3 ± 0.3 nm and a standard deviation of σ_{SAXS} = 1.56 ± 0.02 nm. From the fit to the SAXS data, the thickness of the bilayer membrane was found to be approximately 5 nm, which is concordant with the values obtained in previous atomistic simulations [39]. Note that instrumental smearing was included when fitting the data; the green curve represents the model without smearing and the red curve represents the model with smearing. The SAXS data did not display any signs of multi- or oligo-lamellarity, which would appear as relatively broad additional peaks on top of the main peak. (For interpretation of the references to colour in this figure legend, the reader is referred to the web version of this article.)
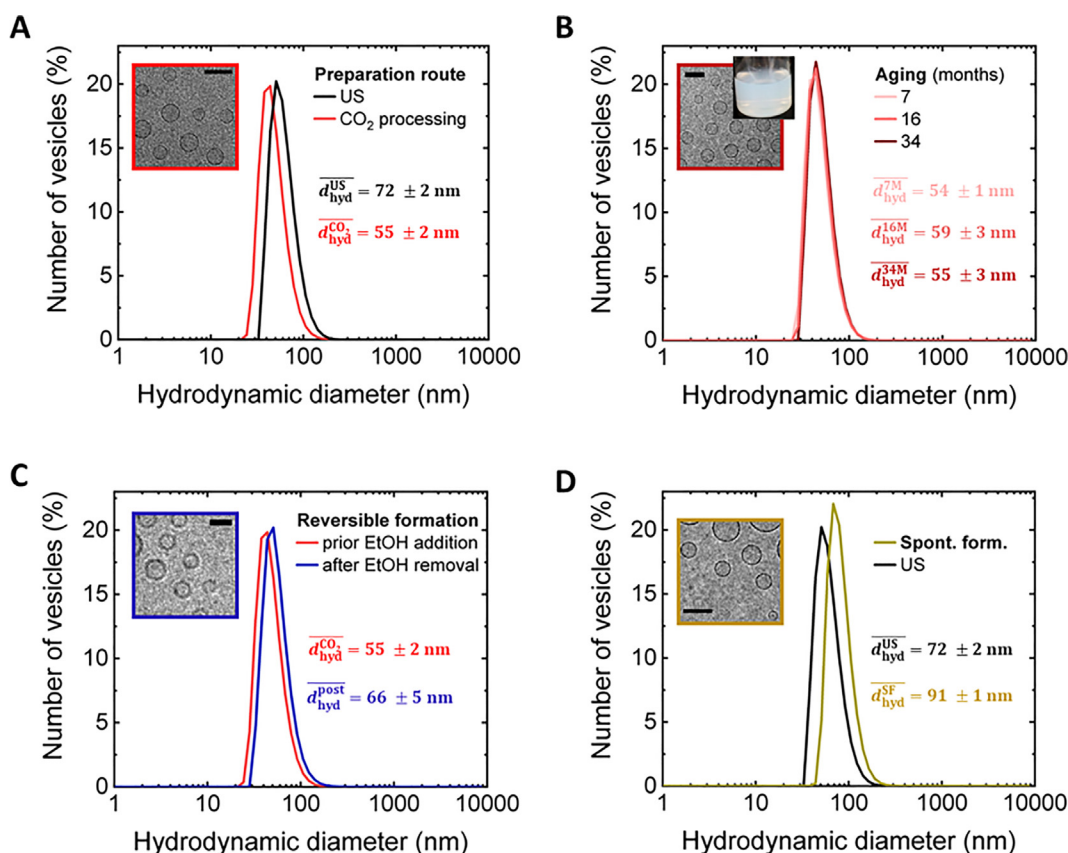
Fig. 3. Experimental evidence indicating that CHOL/CTAB quatsomes are thermodynamically stable. Hydrodynamic diameter distribution of quatsomes under different experimental conditions (with indicated arithmetic mean hydrodynamic diameters $\overline{d_{hyd}}$ ± 1 SD from at least two separate measurements), obtained using dynamic light scattering (DLS) at a concentration of $\sim$ 0.6 mM of each component, and corresponding cryo-TEM images in the inset (scale bars represent 100 nm). (A) Quatsomes obtained using different preparation routes, i.e. through the application of ultrasound (black line) and the depressurization of a CO_2-expanded liquid (red line). (B) Temporal stability of quatsomes over three years. Inset: Cryo-TEM image of quatsomes that have aged for three years, and photograph of the corresponding quatsome suspension, which was completely free of precipitate. (C) Quatsomes as-prepared through the depressurization of a CO_2-expanded liquid (red line), and after ethanol-induced quatsome rupture and subsequent reformation upon ethanol removal (dark blue line). (D) Quatsomes produced through spontaneous formation (dark yellow), i.e. upon gradual addition of a cholesterol solution in EtOH to an aqueous solution containing CTAB micelles, compared to quatsomes formed through the application of ultrasound (black line). (For interpretation of the references to colour in this figure legend, the reader is referred to the web version of this article.)

Table 1

Average values for different structural features of CHOL/CTAB quatsomes in water at 298 K.

Molecular weight (MDa) [a]	Average outer diameter (nm) [b]	Molar ratio CHOL/CTAB [c]	Lipid phase in the bilayer [d]	Equilibrium concentration with CTAB monomers (μM) [e]
13.3 ± 0.8	46.3 ± 0.3	1.11 ± 0.01	Disordered liquid-like packing	< 5

a)Obtained from MALS measurements (Fig. S4).
b)Obtained from SAXS measurements (Fig. 2B).
c)Obtained from HPLC measurements (Table S1).
d)Obtained from WAXS measurements (Fig. S5).
e)Obtained from conductivity measurements (Fig. S8).

obtained through the application of ultrasound (Fig. 3D). The small differences in size may indicate a partially different molecular organization in the vesicular membrane, related to the similar free energies of a cholesterol molecule transferred into a 1:1 bilayer membrane (ΔG = −55 kcal/mol) or a cholesterol nanocrystal (ΔG = −50 kcal/mol) [39], relevant at the later stages of the vesicle formation process [59]. These results suggest that the quatsome formation *per se* does not require any energy supply, but an additional energy input facilitates the formation of CTAB-cholesterol synthons that build up the vesicle membrane.

v) Quatsomes coexist in equilibrium with neighboring single-phase regions in phase diagrams, i.e. *with thermodynamically stable CTAB-rich colloidal assemblies and cholesterol crystals.* The prolonged coexistence of the vesicular quatsome phase with thermodynamically stable CTAB-rich assemblies or cholesterol crystals was observed when cholesterol and CTAB were mixed in non-equimolar ratios; excess of CTAB (e.g. a molar ratio CHOL/CTAB of 1:2) led to the coexistence of CTAB-rich assemblies and quatsomes, as observed using cryo-TEM and isothermal titration calorimetry experiments (see SI, Fig. S7A–C), while an excess of cholesterol (e.g. a molar ratio CHOL/CTAB of 3:2) yielded both unilamellar vesicles and cholesterol crystals (see SI, Fig. S7D).

Finally, to illustrate the resistance of quatsome nanovesicles towards dilutions, we have measured the concentration at which monomerically dissolved CTAB is in equilibrium with the CHOL/CTAB quatsome, and found it to be < 5 μM (see SI, Fig. S8, and Table 1), which is more than two orders of magnitude lower than the critical micelle concentration of CTAB of ∼ 1 mM. Therefore, importantly, the quatsome vesicles are more resistant to dilution than micelles, an important requirement for their use as drug delivery systems [60]. This is consistent with the practically equimolar ratio of CHOL and CTAB even after multiple diafiltrations (Table 1), which implicitly shows that the monomerically dissolved CTAB in equilibrium with the quatsome is practically zero. Moreover, it suggests that the chemical potential of CTAB in the quatsome is much lower than that in the pure micelle, i.e., CTAB in the quatsome is thermodynamically more stable than in the micelle, likely due to the formation of the stable CHOL/CTAB synthon.

4. Conclusions

The data presented here points out that i) CHOL/CTAB quatsomes are thermodynamically stable nanovesicles, and ii) CHOL/CTAB quatsomes are formed through the association of intrinsically planar bilayers in a faceted vesicle with defects. High intermolecular binding energies between CHOL and CTAB hinder the segregation of these two components in the vesicle membrane, and a stable nanovesicle is formed in the absence of major composition asymmetries between the two bilayer leaflets, with a stably persisting lipid density asymmetry.

In particular, coarse-grain molecular dynamics simulations of a complete CHOL/CTAB quatsome demonstrated the absence of spontaneous membrane curvature related to composition asymmetries between the two bilayer leaflets, and instead the presence of planar

bilayer regions joined through defect regions that exhibit strong deformations in the molecular orientation of the membrane components. Experimental observations obtained with cryo-TEM imaging, SAXS, HPLC, MALS, and WAXS, substantiate the simulated results, and further demonstrate a very high vesicle-to-vesicle homogeneity, distinguishing CHOL/CTAB quatsomes from other common nanovesicular structures [61–62]. At the same time, we demonstrate that quatsomes show all the experimental features of a thermodynamically stable vesicle system, with a particularly relevant preparation-route-independent size distribution that is stable over time (monitored along three years). For this demonstration, we have employed different experimental techniques for quatsome production (ultrasound application, depressurization of a CO$_2$-expanded liquid, spontaneous formation) and characterization (DLS, ITC, EPR).

With this data at hand, we propose a novel mechanism underlying the formation of thermodynamically stable nanovesicles, which is based on distortions in the orientation of bilayer molecules in the absence of any segregation of membrane components between the two bilayer leaflets. This mechanism of vesicle formation is different from that proposed thus far for stable vesicular systems (Table 2), based on spontaneous membrane curvature due to composition asymmetry between the two bilayer leaflets [54,21–23], and facilitates the long-term stability of asymmetric lipid densities in the two leaflets, in the absence of the relaxation to symmetric lipid densities through flip-flops between the leaflets described previously [24–25]. In the future, it will be of interest to study the ion distribution across the quatsome membrane, and determine its role in the vesicle stabilization [26–27].

This comprehensive study provides a conceptual framework demonstrating that CHOL/CTAB quatsomes form a stable phase, and it goes well beyond previously published data describing the

Table 2

Formation mechanisms of thermodynamic stable nanovesicles.

Mechanism of nanovesicle formation	Supramolecular organization of nanovesicle bilayer	Experimental examples of thermodynamically stable nanovesicles reported	References
Spontaneous [54,21–23]	membrane curvature	Composition asymmetry between leaflets	Yes
Spontaneous [24–25]	membrane curvature	Asymmetry in lipid density between leaflets	No
Spontaneous [26–27]	membrane curvature	Asymmetric ion concentrations across the membrane	No
Association of This work	intrinsically planar bilayers	Defect regions with distortions in the orientation of bilayer molecules	Yes

structure of these nanovesicles [39] and their use, for example for bioimaging [1–5] and wound healing [9,10]. Furthermore, the study addresses fundamental principles related to the formation of thermodynamically stable nanovesicles with well-defined physico-chemical characteristics and an infinite shelf life, of particular relevance in the development of nanovesicle based products, for example in the pharmaceutical and cosmetics fields.

CRediT authorship contribution statement

Data availability

Data will be made available on request. Simulation data is openly accessible at the ICMAB SoftMatter Theory GitHub repository https://github.com/soft-matter-theory-at-icmab-csic.

Declaration of Competing Interest

The authors declare that they have no known competing financial interests or personal relationships that could have appeared to influence the work reported in this paper.

Acknowledgments

Appendix A. Supplementary data

Supplementary data to this article can be found online at https://doi.org/10.1016/j.jcis.2022.10.104.

References

[1] X. Liu, X. Liu, A. Ardizzone, B. Sui, B. Anzola, N. Ventosa, T. Liu, J. Veciana, K.D. Belfield, Fluorenyl-Loaded Quatsome Nanostructured Fluorescent Probes ACS Omega 2 (8) (2017), pp. 4112–4122, 10.1021/acsomega.7b00779.

[2] D.A. Silbaugh, L. Ferrer-Tasies, J. Faraudo, J. Veciana, N. Ventosa, B.A. Korgel, Highly Fluorescent Silicon Nanocrystals Stabilized in Water Using Quatsomes, Langmuir 33 (50) (2017) 14366–14377, https://doi.org/10.1021/acs.langmuir.7b03539.

[3] A. Ardizzone, S. Kurhuzenkau, S. Illa-Tuset, J. Faraudo, M. Bondar, D. Hagan, E. W. Van Stryland, A. Painelli, C. Sissa, N. Feiner, L. Albertazzi, J. Veciana, N. Ventosa, Nanostructuring Lipophilic Dyes in Water Using Stable Vesicles, Quatsomes, as Scaffolds and Their Use as Probes for Bioimaging, Small 14 (16) (2018) 1703851, https://doi.org/10.1002/smll.201703851.

[4] A. Ardizzone, D. Blasi, D. Vona, A. Rosspeintner, A. Punzi, E. Altamura, N. Grimaldi, S. Sala, E. Vauthey, G.M. Farinola, I. Ratera, N. Ventosa, J. Veciana, Highly Stable and Red-Emitting Nanovesicles Incorporating Lipophilic Diketopyrrolopyrroles for Cell Imaging, Chem. - A Eur. J. 24 (44) (2018) 11386–11392, https://doi.org/10.1002/chem.201801444.

[5] J. Morla-Folch, G. Vargas-Nadal, T. Zhao, C. Sissa, A. Ardizzone, S. Kurhuzenkau, M. Köber, M. Uddin, A. Painelli, J. Veciana, K.D. Belfield, N. Ventosa, Dye-Loaded Quatsomes Exhibiting FRET as Nanoprobes for Bioimaging, ACS Appl. Mater. Interfaces 12 (18) (2020) 20253–20262, https://doi.org/10.1021/acsami.0c03040.

[6] M. Rossetti, L. Stella, J. Morlà-Folch, S. Bobone, A. Boloix, L. Baranda, D. Moscone, M. Roldán, J. Veciana, M.F. Segura, M. Köber, N. Ventosa, A. Porchetta, Engineering DNA-Grafted Quatsomes as Stable Nucleic Acid-Responsive Fluorescent Nanovesicles, Adv. Func. Mater. 31 (2021) 2103511, https://doi.org/10.1002/adfm.202103511.

[7] N. Thomas, D. Dong, K. Richter, M. Ramezanpour, S. Vreugde, B. Thierry, P.-J. Wormald, C.A. Prestidge, Quatsomes for the treatment of Staphylococcus aureus biofilm, J. Mater. Chem. B 3 (2015) 2770–2777, https://doi.org/10.1039/C4TB01953A.

[8] D. Dong, N. Thomas, M. Ramezanpour, A.J. Psaltis, S. Huang, Y. Zhao, B. Thierry, P.-J. Wormald, C.A. Prestidge, S. Vreugde, Inhibition of Staphylococcus aureus and Pseudomonas aeruginosa biofilms by quatsomes in low concentrations, Exp. Biol. Med. 245 (1) (2020) 34–41, https://doi.org/10.1177/1535370219896779.

[9] H. J. Santana Milián, N. Ventosa, E. Martínez Díaz, J. Berlanga Acosta, I. Cabrera, J. Veciana, Vesicles comprising epidermal growth factor and compositions there of WO/2014/019555 (2014).

[10] L. Ferrer-Tasies, H. Santana, I. Cabrera-Puig, E. González-Mira, L. Ballell-Hosa, C. Castellar-Álvarez, A. Córdoba, J. Merlo-Mas, H. Gerónimo, G. Chinea, V. Falcón, E. Moreno-Calvo, J. S. Pedersen, J. Romero, C. Navarro-Requena, C. Valdés, M. Limonta, J. Berlanga, S. Sala, E. Martínez, J. Veciana, N. Ventosa, Recombinant Human Epidermal Growth Factor/Quatsome Nanoconjugates: A Robust Topical Delivery System for Complex Wound Healing Adv. Ther. 4 (6) (2021), 2000260, 10.1002/adtp.202000260.

[11] A. Boloix, N. Feiner-Gracia, M. Köber, J. Repetto, R. Pascarella, A. Soriano, M. Masanas, N. Segovia, G. Vargas-Nadal, J. Merlo-Mas, D. Danino, I. Abutbul-Ionita, L. Foradada, J. Roma, A. Córdoba, S. Sala, J. Sánchez de Toledo, S. Gallego, J. Veciana, L. Albertazzi, M.F. Segura, N. Ventosa, Engineering pH-sensitive stable nanovesicles for delivery of miRNA therapeutics, Small 18 (3) (2022) 2101959, https://doi.org/10.1002/smll.202101959.

[12] I. Cabrera, E. Elizondo, O. Esteban, J.L. Corchero, M. Melgarejo, D. Pulido, A. Córdoba, E. Moreno, U. Unzueta, E. Vazquez, I. Abasolo, S. Schwartz, A. Villaverde, F. Albericio, M.F. García-Parajo, N. Ventosa, J. Veciana, Multifunctional Nanovesicle-Bioactive Conjugates Prepared by a One-Step Scalable Method Using CO2-Expanded Solvents, Nano Lett. 13 (8) (2013) 3766–3774, https://doi.org/10.1021/nl4017072.

[13] G. Vargas-Nadal, M. Muñoz-Úbeda, P. Álamo, M. Mitjans, V. Céspedes, M. Köber, E. González-Mira, L. Ferrer-Tasies, M. P. Vinardell, R. Mangues, J. Veciana, N. Ventosa, MKC-Quatsomes: a stable nanovesicle platform for bio-imaging and drug-delivery applications, Nanomed. Nanotechnol., Biol. Med. 24 (2020), 102136, http://doi.org/10.1016/j.nano.2019.102136.

[14] E.F. Marques, Size and Stability of Catanionic Vesicles: Effects of Formation Path, Sonication, and Aging, Langmuir 16 (11) (2000) 4798–4807, https://doi.org/10.1021/la9908135.

[15] M. Antonietti, S. Förster, Vesicles and Liposomes: A Self-Assembly Principle Beyond Lipids, Adv. Mater. 15 (16) (2003) 1323–1333, https://doi.org/10.1002/adma.200300010.

[16] V. Guida Thermodynamics and kinetics of vesicles formation processesAdv. Colloid Interface Sci. 161 (1–2) (2010), pp. 77–88, http://doi.org/10.1016/j.cis.2009.11.004.

[17] E.W. Kaler, A.K. Murthy, B.E. Rodriguez, J.A.N. Zasadzinski, Spontaneous Vesicle Formation in Aqueous Mixtures of Single-Tailed Surfactants, Science 245 (4924) (1989) 1371–1374, https://doi.org/10.1126/science.2781283.

[18] E.W. Kaler, K.L. Herrington, A.K. Murthy, J.A.N. Zasadzinski, Phase behavior and structures of mixtures of anionic and cationic surfactants, J. Phys. Chem. 96 (16) (1992) 6698–6707, https://doi.org/10.1021/j100195a033.

[19] C.-Y. Leung, L.C. Palmer, S. Kewalramani, B. Qiao, S.I. Stupp, M. Olvera de la Cruz, M.J. Bedzyk, Crystalline polymorphism induced by charge regulation in ionic membranes Proc, Natl. Acad. Sci. 110 (41) (2013) 16309–16314, https://doi.org/10.1073/pnas.131615011.

[20] C.-Y. Leung, L.C. Palmer, B. Fu Qiao, S. Kewalramani, R. Sknepnek, C.J. Newcomb, M.A. Greenfield, G. Vernizzi, S.I. Stupp, M.J. Bedzyk, M. Olvera de la Cruz, Molecular Crystallization Controlled by pH Regulates Mesoscopic Membrane Morphology, ACS Nano 6 (12) (2012) 10901–10909, https://doi.org/10.1021/nn304321w.

[21] S.A. Safran, P. Pincus, D. Andelman, Theory of Spontaneous Vesicle Formation in Surfactant Mixtures, Science 248 (4953) (1990) 354–356, https://doi.org/10.1126/science.248.4953.354.

[22] S.A. Safran, P.A. Pincus, D. Andelman, F.C. MacKintosh, Stability and phase behavior of mixed surfactant vesicles Phys, Rev. A 43 (1991) 1071–1078, https://doi.org/10.1103/PhysRevA.43.1071.

[23] M.L. Strader, H.B. de Aguiar, A.G.F. de Beer, S. Roke, Label-free spectroscopic detection of vesicles in water using vibrational sum frequency scattering, Soft Matter 7 (2011) 4959–4963, https://doi.org/10.1039/C0SM01358G.

[24] B. Różycki, R. Lipowsky, Spontaneous Curvature of bilayer membranes from molecular simulations: Asymmetric lipid densities and asymmetric adsorption, J. Chem. Phys. 142 (2015), https://doi.org/10.1063/1.4906149.

[25] A. Hossein, M. Deserno, Spontaneous Curvature, Differential Stress, and Bending Modulus of Asymmetric Lipid Membranes, Biophys. J. 118 (3) (2020) 624–642, https://doi.org/10.1016/j.bpj.2019.11.3398.

[26] B. Różycki, R. Lipowsky, Membrane curvature generated by asymmetric depletion layers of ions, small molecules, and nanoparticles, J. Chem. Phys. 145 (2016), https://doi.org/10.1063/1.4960772.

[27] M. Karimi, J. Steinkühler, D. Roy, R. Dasgupta, R. Lipowsky, R. Dimova, Asymmetric Ionic Conditions Generate Large Membrane Curvatures, Nano Lett. 18 (12) (2018) 7816–7821, https://doi.org/10.1021/acs.nanolett.8b03584.

[28] D. Van Der Spoel, E. Lindahl, B. Hess, G. Groenhof, A.E. Mark, H.J.C. Berendsen, GROMACS: Fast, flexible, and free, J. Comput. Chem. 26 (16) (2005) 1701–1718, https://doi.org/10.1002/jcc.20291.

[29] B. Hess, C. Kutzner, D. Van Der Spoel, E. Lindahl, GROMACS 4: Algorithms for highly efficient, load-balanced, and scalable molecular simulation, J. Chem. Theory Comput. 4 (3) (2008) 435–447, https://doi.org/10.1021/ct700301q.

[30] S. Pronk, S. Páll, R. Schulz, P. Larsson, P. Bjelkmar, R. Apostolov, M.R. Shirts, J.C. Smith, P.M. Kasson, D. van der Spoel, B. Hess, E. Lindahl, GROMACS 4.5: A high-throughput and highly parallel open source molecular simulation toolkit, Bioinformatics 29 (7) (2013) 845–854, https://doi.org/10.1093/bioinformatics/btt055.

[31] M.J. Abraham, T. Murtola, R. Schulz, S. Páll, J.C. Smith, B. Hess, E. Lindahl, Gromacs: High performance molecular simulations through multi-level parallelism from laptops to supercomputers, SoftwareX 1–2 (2015) 19–25, https://doi.org/10.1016/j.softx.2015.06.001.

[32] C. Arnarez, J.J. Uusitalo, M.F. Masman, H.I. Ingólfsson, D.H. de Jong, M.N. Melo, X. Periole, A.H. de Vries, S.J. Marrink, Dry Martini, a Coarse-Grained Force Field for Lipid Membrane Simulations with Implicit Solvent, J. Chem. Theory Comput. 11 (1) (2015) 260–275, https://doi.org/10.1021/ct500477k.

[33] S. Illa-Tuset, D.C. Malaspina, J. Faraudo, Coarse-grained molecular dynamics simulation of the interface behaviour and self-assembly of CTAB cationic surfactants, Phys. Chem. Chem. Phys. 20 (2018), pp. 26422–26430, 10.1039/C8CP04505D.

[34] Y. Qi, H.I. Ingólfsson, X. Cheng, J. Lee, S.J. Marrink, W. Im, CHARMM-GUI Martini Maker for Coarse-Grained Simulations with the Martini Force Field, J. Chem. Theory Comput. 11 (9) (2015) 4486–4494, https://doi.org/10.1021/acs.jctc.5b00513.

[35] P.C. Hsu, B.M.H. Bruininks, D. Jefferies, P.C. Telles de Souza, J. Lee, D.S. Patel, S.J. Marrink, Y. Qi, S. Khalid, W. Im, CHARMM-GUI Martini Maker for modeling and simulation of complex bacterial membranes with lipopolysaccharides, J. Comput. Chem. 38 (27) (2017) 2354, https://doi.org/10.1002/jcc.24895.

[36] G. Bussi, D. Donadio, M. Parrinello, Canonical sampling through velocity rescaling, J. Chem. Phys. 126 (1) (2007), https://doi.org/10.1063/1.2408420.

[37] W. Humphrey, A. Dalke, K. Schulten, VMD: Visual molecular dynamics, J. Mol. Graph. 14 (1) (1996) 33–38, https://doi.org/10.1016/0263-7855(96)00018-5.

[38] N. Ventosa, J. Veciana, S. Sala, M. Cano, Method for obtaining micro- and nano-disperse systems WO 2006/079889 (2005).

[39] L. Ferrer-Tasies, E. Moreno-Calvo, M. Cano-Sarabia, M. Aguilella-Arzo, A. Angelova, S. Lesieur, S. Ricart, J. Faraudo, N. Ventosa, J. Veciana, Quatsomes: Vesicles Formed by Self-Assembly of Sterols and Quaternary Ammonium Surfactants, Langmuir 29 (22) (2013) 6519–6528, https://doi.org/10.1021/la4003803.

[40] D. Danino, Cryo-TEM of soft molecular assemblies, Curr Opin. Colloid Interface Sci. 17 (6) (2012) 316–329, https://doi.org/10.1016/j.cocis.2012.10.003.

[41] J.S. Pedersen, A flux- and background-optimized version of the NanoSTAR small-angle X-ray scattering camera for solution scattering, J. Appl. Crystallogr. 37 (3) (2004) 369–380, https://doi.org/10.1107/S0021889804004170.

[42] J. Lyngsø, J.S. Pedersen, A high-flux automated laboratory small-angle X-ray scattering instrument optimized for solution scattering, J. Appl. Crystallogr. 54 (2021) 295–305, https://doi.org/10.1107/S1600576720016209.

[43] A. Schwamberger, B. De Roo, D. Jacob, L. Dillemans, L. Bruegemann, J.W. Seo, J. P. Locquet, Combining SAXS and DLS for simultaneous measurements and time-resolved monitoring of nanoparticle synthesis, Nucl. Instrum. Methods Phys. Res. Sect. B Beam Interact. Mater. Atoms. 343 (2015) 116–122, https://doi.org/10.1016/j.nimb.2014.11.049.

[44] Y. Li, R. Beck, T. Huang, M.C. Choi, M. Divinagracia, Scatterless hybrid metal-single-crystal slit for small-angle X-ray scattering and high-resolution X-ray diffraction, J. Appl. Crystallogr. 41 (6) (2008) 1134–1139, https://doi.org/10.1107/S0021889808031129.

[45] J.S. Pedersen, X-ray analyzing system for x-ray scattering analysis US20140270079A1 (2014).

[46] J.S. Pedersen, Analysis of small-angle scattering data from colloids and polymer solutions: Modeling and least-squares fitting, Adv. Colloid Interface Sci. 70 (1997) 171–210, https://doi.org/10.1016/S0001-8686(97)00312-6.

[47] J.S. Pedersen, M.C. Gerstenberg, The structure of P85 Pluronic block copolymer micelles determined by small-angle neutron scattering, Colloids Surfaces A Physicochem. Eng. Asp. 213 (2–3) (2003) 175–187, https://doi.org/10.1016/S0927-7757(02)00511-3.

[48] J.S. Pedersen, D. Posselt, K. Mortensen, Analytical treatment of the resolution function for small-angle scattering, J. Appl. Crystallogr. 23 (4) (1990) 321–333, https://doi.org/10.1107/S0021889890003946.

[49] X. Li, C.-Y. Shew, L. He, F. Meilleur, D.A.A. Myles, E. Liu, Y. Zhang, G.S. Smith, K. W. Herwig, R. Pynn, W.-R. Chen, Scattering functions of Platonic solids, J. Appl. Crystallogr. 44 (3) (2011) 545–557, https://doi.org/10.1107/S0021889811011691.

[50] P. Kratochvíl, Classical light scattering from polymer solutions, Elsevier, 1987.

[51] A.F. Brandner, S. Timr, S. Melchionna, P. Derreumaux, M. Baaden, F. Sterpone, Modelling lipid systems in fluid with Lattice Boltzmann Molecular Dynamics simulations and hydrodynamics, Sci. Rep. 9 (1) (2019) 1–14, https://doi.org/10.1038/s41598-019-52760-y.

[52] B. Gumí-Audenis, S. Illa-Tuset, N. Grimaldi, L. Pasquina-Lemonche, L. Ferrer-Tasies, F. Sanz, J. Veciana, I. Ratera, J. Faraudo, N. Ventosa, M.I. Giannotti, Insights into the structure and nanomechanics of a quatsome membrane by force spectroscopy measurements and molecular simulations, Nanoscale 10 (2018) 23001–23011, https://doi.org/10.1039/C8NR07110A.

[53] R. Ghosh, V. Satarifard, A. Grafmüller, R. Lipowsky, Spherical Nanovesicles Transform into a Multitude of Nonspherical Shapes, Nano Lett. 19 (11) (2019) 7703–7711, https://doi.org/10.1021/acs.nanolett.9b02646.

[54] H.T. Jung, B. Coldren, J.A. Zasadzinski, D.J. Iampietro, E.W. Kaler, The origins of stability of spontaneous vesicles Proc, Natl. Acad. Sci. 98 (4) (2001) 1353–1357, https://doi.org/10.1073/pnas.98.4.1353.

[55] G. Milcovich, F.E. Antunes, M. Grassi, F. Asaro, Stabilization of unilamellar catanionic vesicles induced by β-cyclodextrins: A strategy for a tunable drug delivery depot, Int. J. Pharm. 548 (1) (2018) 474–479, https://doi.org/10.1016/j.ijpharm.2018.07.026.

[56] The average bilayer volume was calculated for an outer vesicle radius of 20.65 nm and a total bilayer thickness of 5 nm, both mean values obtained from SAXS.

[57] D.I. Svergun, M.H.J. Koch, Small-angle scattering studies of biological macromolecules in solution Reports, Prog. Phys. 66 (10) (2003) 1735–1782, https://doi.org/10.1088/0034-4885/66/10/R05.

[58] J.M. Teulon, C. Godon, L. Chantalat, C. Moriscot, J. Cambedouzou, M. Odorico, J. Ravaux, R. Podor, A. Gerdil, A. Habert, N. Herlin-Boime, S.-W.-W. Chen, J.-L. Pelleguer, On the Operational Aspects of Measuring Nanoparticle Sizes, Nanomaterials 9 (1) (2019) 18, https://doi.org/10.3390/nano9010018.

[59] The free energy of a cholesterol molecule transferred to a CTAB micelle, relevant at the initial stages of the formation process, is ΔG = -81 kcal/mol.

[60] Y. Lu, E. Zhang, J. Yang, Z. Cao, Strategies to improve micelle stability for drug delivery, Nano Res. 11 (2018) 4985–4998, https://doi.org/10.1007/s12274-018-2152-3.

[61] J.E. Nielsen, V.A. Bjørnestad, R. Lund, Resolving the structural interactions between antimicrobial peptides and lipid membranes using small-angle scattering methods: the case of indolicidin, Soft Matter 14 (2018) 8750, https://doi.org/10.1039/C8SM01888J.

[62] C.-A. Wang, Y.-Q. Yeh, C.-Y. Mou, C.-J. Su, W.-R. Wu, U.-S. Jeng, Small-angle-scattering resolved catanionic unilamellar vesicles as molecule carriers, Mater. Chem. Phys. 277 (2022), https://doi.org/10.1016/j.matchemphys.2021.125435 125435.